The Countervailing Obliquity–Precession Effect: A Biannual Insolation Asymmetry that Preconditions the Climate System

John A. Parmentola
2777 Paradise Road
Las Vegas, NV 89109

Version 1 - April 2026
Preprint. https://doi.org/10.5281/zenodo.19825774

Abstract

Orbital variations distribute solar radiation across the top of the atmosphere while leaving the global annual solar input nearly constant over millennial timescales. The mechanisms by which this distribution influences glacial–interglacial climate evolution, however, remain incompletely understood. This study identifies a countervailing structure in orbital forcing arising from the combined effects of declining obliquity and the precessional migration of the seasonal cycle relative to perihelion and aphelion. This mechanism, referred to here as the Countervailing Obliquity–Precession Effect (COPE), produces a biannual asymmetry in the insolation and energy deposition between two six-monthly orbital segments that evolve predictably over time in a measurable way.

The climatic consequences of COPE depend strongly on latitude and material regime. In the tropical zone (TZ), solar energy input accumulates, influencing long-term temperature trends, evaporation, and ocean heat content. During the Holocene, TZ insolation averaged over six successive monthly orbital segments reached a minimum approximately 4.6 kyr ago and has since increased monotonically. The associated tropical energy input at the top of the atmosphere over the next century, relative to this minimum, is approximately 6.5×10^{24} J, resulting from the two six-monthly orbital segments, sufficient to influence upper-ocean temperatures on centennial timescales. Expressed annually, this COPE energy deposition corresponds to the latent heat required to evaporate roughly 5% of the global annual precipitation. In contrast, the Arctic zone (AZ) response is governed not by cumulative energy but by melt-season insolation trends reflecting the temperature threshold required for ice melt. AZ summer-season average insolation has declined by more than 30 W/m² from its early-Holocene maximum and shows no recovery over several millennia, while winter-season insolation remains comparatively negligible.

COPE therefore establishes a countervailing energy structure in which rising tropical energy input coexists with declining Arctic melt-season forcing. Satellite observations from the CERES mission reveal a persistent tropical top-of-atmosphere (TOA) time-averaged radiative asymmetry of approximately 1 W/m², indicating that the tropical climate system retains a climatically significant fraction of the imposed seasonal orbital forcing after compensation by cloud reflection and longwave emission. The same countervailing insolation structure is present during MIS 19c, demonstrating that COPE is a common orbital forcing precondition for both the present interglacial (MIS 1) and its closest orbital analog.

Because COPE follows directly from orbital dynamics, Earth's geometry, and solar radiative transfer—with no adjustable parameters—it provides a physically transparent framework in which orbital forcing produces a biannual asymmetry in tropical energy deposition that establishes boundary conditions for the tropical energy reservoir and Arctic melt regime, thereby providing preconditions for the hydrological cycle, the meridional temperature gradient, poleward moisture transport, and the potential for glaciation.

1. Introduction

In a previous paper (Parmentola, J.A., 2023), we showed that rare synchronizations between the precession index (precession modulated by eccentricity) and obliquity coincide with interglacial inceptions and terminations over the past ~800,000 years. These results reinforce the standard Milankovitch hypothesis (Milankovitch, M., 1941) regarding the orbital pacing of glacial–interglacial transitions (Hays, J.D., Imbrie, J. and Shackleton, N.J., 1976). That analysis, however, did not explicitly identify the physical mechanism by which orbital geometry produces concurrent warming and cooling in different regions of the Earth's climate system to support glaciation. The present study examines the climatic implications of orbital forcing by analyzing the seasonal partitioning of insolation and solar energy between the TZ and AZ.

The estimated 400-ft decline in global sea levels during ice ages (Fairbanks, R.,1989) implies substantial prior evaporation of ocean water, providing empirical evidence of warming. The energy required to evaporate this volume of water is large, on the order of 1×10^{26} J. A central question of this research is whether orbital geometry alone can supply the solar energy deposited within a latitudinal zone over a precessional half-cycle (~11 kyr), or a significant fraction thereof, to meet or exceed the energy evaporation requirement without climate feedback effects.

Variations in average solar irradiance associated with solar cycles appear far too small to account for the required energy. And while a secular decline in obliquity over the past ~10 kyr shifts the latitude of peak insolation equatorward while increasing TZ insolation intensity, this effect alone is comparatively small, as shown previously (Parmentola, J.A., 2023). Nevertheless, because the TZ receives the most intense solar radiation, it is the likely region for such evaporation, as we will demonstrate later.

The global mean annual insolation has remained close to 342 W/m² for millions of years, with variations on the order of ~0.1 W/m². Figure 1 illustrates this near constancy over the interval −1 to +1 Myr, computed using the methodology described in Appendix A. The small deviations from constancy arise because of the many-body forces acting on the Earth.

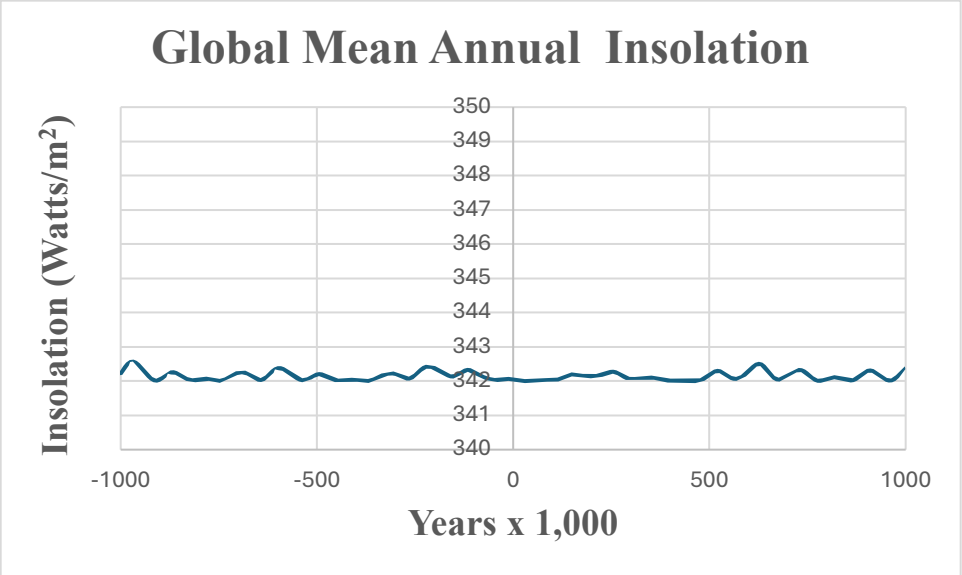

Figure 1. Global mean annual insolation computed using the method described in Appendix A.

While Figure 1 demonstrates the stability of the global annual mean, it does not capture how solar energy is distributed in time or latitude, nor how energy accumulates within the Earth's climate system. Other averages—daily, monthly, or zonal—reveal pronounced seasonal and latitudinal structure, with some variations of hundreds of W/m². Global averaging mutes the details of the structural forcings, but the Earth does not experience the average; it receives solar energy as it arrives in time and space. The approximate energy constancy does not apply separately to latitudinal zones where insolation and energy deposition can vary quite significantly over the seasons. The classic example of this is the AZ, where the average summer season insolation has declined by more than 30 W/m^2 over the last 11,000 years, while winter insolation has remained comparatively low and constant. From the global annual constancy of energy deposited, this AZ cooling implies that there must be heating somewhere else, a countervailing effect at the TOA that is an input into the climate system.

For the two-body problem, the global annual mean insolation is constant. The orbit also exhibits a biannual symmetry: when divided by the major axis, the global mean insolation in each half of the orbit is identical. This symmetry does not hold when the orbit is divided by the minor axis. This feature follows from Kepler's Second Law. More importantly, this symmetry is entirely broken for an elliptical orbit when insolation is averaged annually at a latitude or over a latitude zone, because the projection of solar radiation onto the tilted Earth introduces strong seasonal dependence. This inherent latitudinal asymmetry arises from Earth's elliptical orbit due to the sun's position. As Earth moves from aphelion toward perihelion, solar energy delivery intensifies; as it returns from perihelion to aphelion, it weakens. Concurrently, the axial precession causes the calendar months to drift along this asymmetric orbit on kiloyear timescales, so that the seasons do not occur at fixed heliocentric distances. The calendar months would be fixed in orbital longitude only if the precession were absent.

Figure 2 illustrates this drift by comparing Earth's orbital configuration today with that of ~11,000 years ago.

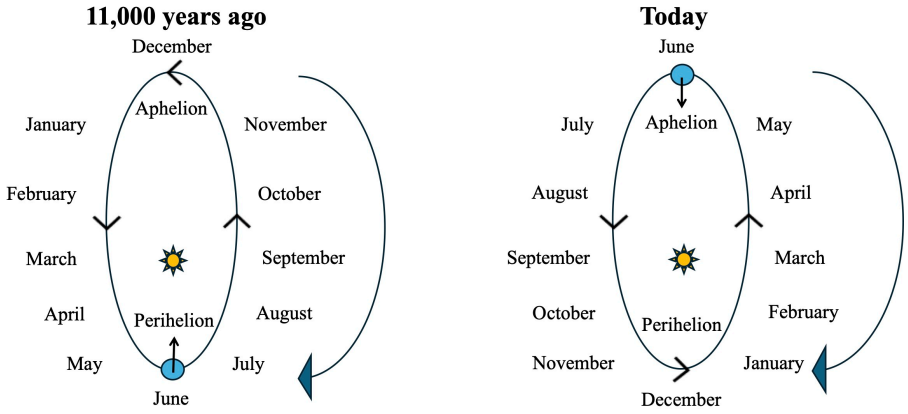

Figure 2. Approximately 11,000 years ago, the June solstice occurred near perihelion (left), whereas today it occurs near aphelion (right). Earth moves counterclockwise around its orbit, while the calendar months migrate clockwise due to the precession.

As Figure 2 indicates, the summer solstice always occurs in June by definition, but it does not occur at a fixed orbital longitude. Because the months drift relative to Earth's elliptical orbit, they sample different heliocentric distances and therefore different solar intensities over time.

The physical consequence of this orbital geometry is a Countervailing Obliquity–Precession Effect (COPE). A secular decline in obliquity reduces summer solar elevation at high latitudes, suppressing AZ summer insolation and melt potential, while simultaneously increasing insolation intensity in the TZ as the zenith of latitude shifts southward. Over a precession half-cycle, axial precession moves the summer,

spring, and early-winter months through perihelion toward aphelion, initially increasing solar intensity to a maximum by reducing Earth–Sun distance, and then a subsequent decline to a minimum in the future. At the same time, the winter, spring, and early summer months move initially through aphelion toward perihelion, reducing solar intensity to a minimum by increasing the Earth-Sun distance, then increasing it through the present to a maximum in the future. These effects are significant in the tropics, where solar rays are nearly normal to the surface and constitute a purely geometric, out-of-phase bifurcation of the insolation into two channels. Thus, obliquity and precession act in a countervailing manner across latitudes: both contribute to TZ warming while cooling the AZ.

The climatic response to COPE depends on the material regime. In the TZ, solar input accumulates as energy, governing ocean heat content, evaporation, poleward moisture transport, and convection. In the AZ, the climate response is controlled not by cumulative energy but by melt-season insolation trends, reflecting the temperature threshold required for ice melt. Global annual averaging mutes this countervailing structure by creating an apparent cyclical symmetry that orbital mechanics explicitly breaks within zones and across seasons.

Although COPE operates globally, the present analysis focuses on the zonal energetics of the tropical band, which spans both hemispheres and therefore captures the dominant component of low-latitude energy throughput, given its comparatively high mean insolation. Southern Hemisphere processes contribute to the maintenance of the near-uniform annual tropical insolation and participate in the cross-equatorial adjustments of the Hadley Cell circulation, but explicit hemispheric decomposition is not required to establish the COPE mechanism here.

In contrast to the TZ, midlatitudes receive substantial summer season insolation, but radiation losses from autumn to winter limit long-term energy accumulation. Because sustained forcing integrates more effectively than intermittent forcing, low-latitude energy anomalies possess disproportionate thermodynamic leverage, hence the emphasis on the TZ.

Furthermore, the TZ has a surface area four times that of the subtropical zone (STZ), making the STZ's role as an energy reservoir less significant than that of the TZ. This conclusion is supported by explicit computations that place its energy-deposition effect at about 20% of the TZ's over the same duration.

Finally, the TZ surface area is six times that of the AZ, where the inherent shallow angles of the sun's rays make it persistently cold, especially during the winter season.

Hence, the present analysis focuses on the TZ and AZ because these regions define the primary thermodynamic endpoints of the climate system: low latitudes constitute the principal region of net energy gain and ocean-atmosphere coupling, while high latitudes govern melt-season persistence and net radiation loss to space. Midlatitude and subtropical bands, though dynamically important as pathways of poleward energy transport, do not dominate the acquisition of solar energy or the principal influence of cryospheric mass balance. Accordingly, the countervailing structure described here is evaluated between these two zonal thermodynamic endpoints.

The individual effects of obliquity and precession on insolation have long been recognized within the Milankovitch framework. The present analysis emphasizes that when these effects are examined through zonal and seasonal energy partitions, their combined action produces a countervailing distribution of solar energy at the TOA between tropical and Arctic regions. This coupled behavior provides a compact physical description of how orbital geometry influences the reorganization of the seasonal energy balance over time while the global annual energy input remains nearly constant. Orbital variations determine the spatial and seasonal distribution of insolation but do not redistribute energy within the climate system; that redistribution occurs through atmospheric and oceanic dynamics.

The conventional interpretation of orbital forcing assumes that the near constancy of global annual mean insolation implies negligible long-term radiative forcing. Under this interpretation, variations in Earth's orbital parameters influence climate primarily through localized seasonal effects, particularly summer insolation at high northern latitudes.

The present study tests the alternative hypothesis that orbital variations distribute solar energy seasonally and latitudinally, producing persistent thermodynamic asymmetries even when the global annual mean remains nearly constant. In particular, the Countervailing Obliquity–Precession Effect (COPE) proposes that two complementary six-monthly-period tropical energy channels evolve in opposite directions over time.

The objective of this paper is to establish the physical basis of COPE and to quantify some of its consequences. In addition to assessing its general thermodynamic consequences, we apply this framework to MIS 1 and MIS 19c to further establish their similarity and to determine whether orbital geometry alone could, in principle, supply the energy required to lower global sea level by ~400 ft. We further show that satellite measurements from the CERES mission reveal a persistent tropical seasonal top-of-atmosphere radiative asymmetry that results in a net average gain into the TZ of approximately 1 W/m² due to COPE over the past two decades, indicating that the tropical system retains a climatically significant fraction of the seasonal COPE orbital forcing after accounting for cloud reflection and longwave emission. These results follow directly from orbital geometry, Newtonian mechanics, standard General Relativistic corrections, Earth's spheroidal geometry, and solar ray optics, without adjustable parameters or numerical climate models.

In Section 2, we discuss the physical basis of the COPE framework. In Section 3, we present the key equations used to compute insolation and energy deposition by latitudinal zone, monthly period, and season. In Section 4, we compute the COPE consequences for the AZ and TZ. In Section 5, we present the COPE comparison of MIS1 and MIS19c. In Section 6, we explore whether the biannual asymmetry induced by COPE persists under climate feedback mechanisms using CERES data. The summary and discussion are presented in Section 7.

---

2. Physical Basis: Modulated Solar Energy as a Wave

Solar irradiance (≈1368 W m^{-2}) is a spatially uniform signal incident on the Earth. Earth's orbital and celestial motions modulate this signal, producing insolation distributed over the planet's surface and forming an amplitude-modulated wave analogous to an AM radio signal. The energy deposited through this insolation is therefore also wave-like, reflecting the combined effects of orbital geometry and temporal integration.

Insolation, like solar irradiance, is an instantaneous power density and therefore an intensive quantity. As such, it primarily governs spatial temperature contrasts across seasons and latitudinal zones. The energy deposited by that insolation, obtained by integrating power over time, is an extensive and cumulative quantity. It is this accumulated energy that governs temperature trends and long-term climate evolution. Analyses based solely on insolation implicitly emphasize spatial structure while muting the temporal accumulation of energy that drives climate change. In later sections, we elaborate on these physically distinct roles.

At the present epoch, the seasonal calendar occupies a geometric configuration: six-monthly periods (see Appendix A for a definition of monthly periods) lie predominantly on the energy-increasing side of Earth's elliptical orbit, while the remaining six-monthly periods lie on the energy-decreasing side. This

configuration bifurcates seasonal energy deposition into two distinct channels associated with opposite sides of the orbital major axis. Within latitudinal zones, these channels represent inequivalent pathways of energy delivery that accumulate within the Earth system as insolation is integrated over time.

The channel structure evolves because Earth receives varying amounts of solar energy across monthly periods and latitudes. Axial precession causes the monthly windows to drift along the orbit, altering their heliocentric distances and, therefore, the insolation they receive. Each monthly period thus possesses a distinct precessional phase. And Kepler's Second Law implies that the number of days in each monthly period is not constant. Variable monthly-period days will be used in subsequent computations, following the method described in Appendix B.

For the first set of six successive-monthly periods, each period exhibits an insolation minimum at some point over the past ~11 kyr, and each minimum corresponds to the initiation of an increasing energy-accumulation channel. These monthly period energy contributions overlap in epochal time and produce a constructive energy-accumulation wave at the TOA. For the second set of six-monthly periods, a corresponding set of insolation maxima initiates declining energy-accumulation channels, which likewise overlap. The resulting behavior is a superposition of phase-shifted energy waves.

In the next section, we present the method for computing the temporal accumulation of energy within latitudinal zones according to the COPE mechanism.

---

3. The Framework for Energy Deposited into Latitudinal Zones at the TOA

In this section, we present the relevant equations for determining the energy deposited into latitudinal zones at the TOA. The general expression for the latitude-zone mean monthly insolation is given by

$$\tilde{Q}_{LZ,i}(t) = \frac{\int_{\emptyset_1}^{\emptyset_2} Q_i(\emptyset,t)\cos(\emptyset)d\emptyset}{\int_{\emptyset_1}^{\emptyset_2} \cos(\emptyset)d\emptyset} \quad (2.1)$$

, where $Q_i(\emptyset, t)$ is the mean monthly-period insolation at time, t, and latitude, $\emptyset$, computed using the methodology described in Appendix A. The index, *i,* refers to a monthly period as defined in Appendix A, *LZ* is the latitude zone, and $\emptyset_1$ *and* $\emptyset_2$ are the angular limits of the *LZ*. The boxcar average of the *LZ* mean insolation over monthly periods of interest is given by

$$\bar{Q}_{LZ}(t) = \sum_i w_i \cdot \tilde{Q}_{LZ,i}(t) \quad (2.2)$$

, where w_i the monthly period weighting factor is defined as

$$w_i = \frac{\Delta t_i}{T} \quad (2.3)$$

, where Δt_i is a monthly period duration, which, because of Kepler's Second Law, is not fixed, and $T = \sum_i \Delta t_i$ is the sum over monthly periods of interest. For the entire year, T is fixed at 365.2422 days. The quantities $\Delta t_i\ \tilde{Q}_{LZ,i}(t)$ in equation (2.2) are the monthly period energies deposited within *LZ* at the *TOA*,

and their summation represents the superposition of energy deposition waves. The average power at epochal time, t, into an LZ is given by

$$\bar{P}_{LZ}(t) = A_{LZ}\ \bar{Q}_{LZ}(t) \tag{2.4}$$

, where A_{LZ} is the latitudinal area of interest at the *TOA*. Finally, the total average energy deposited into an *LZ* at the *TOA* is given by

$$\bar{E}_{LZ}(t_1, t_2) = \int_{t_1}^{t_2} \bar{P}_{LZ}(t)\, dt \cdot \Delta T \tag{2.5}$$

, where t_1 and t_2 represent the epochal duration over which the energy is deposited.

These are the primary equations, together with the computational methodology described in Appendices A and B, that will be used to explore the energy-deposition effects of COPE within *LZs*, establish the physical relationship between the interglacial MIS1 and MIS19c, and determine if the estimated energy deposited over the precession half-cycle or fraction thereof, in principle, meets or exceeds the requirement of lowering sea levels by 400 feet.

In the next section, we demonstrate COPE computationally.

---

4. Countervailing Distribution of Insolation through Orbital Geometry

As Figure 2 above suggests, there is a natural separation of the insolation into two out-of-phase channels due to the Earth's asymmetric energy gain along its elliptic orbit. The two channels are six-monthly periods per Appendix A, designated 2-7, involving six minima that all occur before t=0 (year 2000), and those monthly periods, 8-12+1, with corresponding maxima that also occur before t=0. These insolation curves are obtained from equation (2.1) by integrating the mean monthly insolation over the TZ latitudes from -23.4393 to +23.4393 degrees and are depicted in Figures 3 and 4 below:

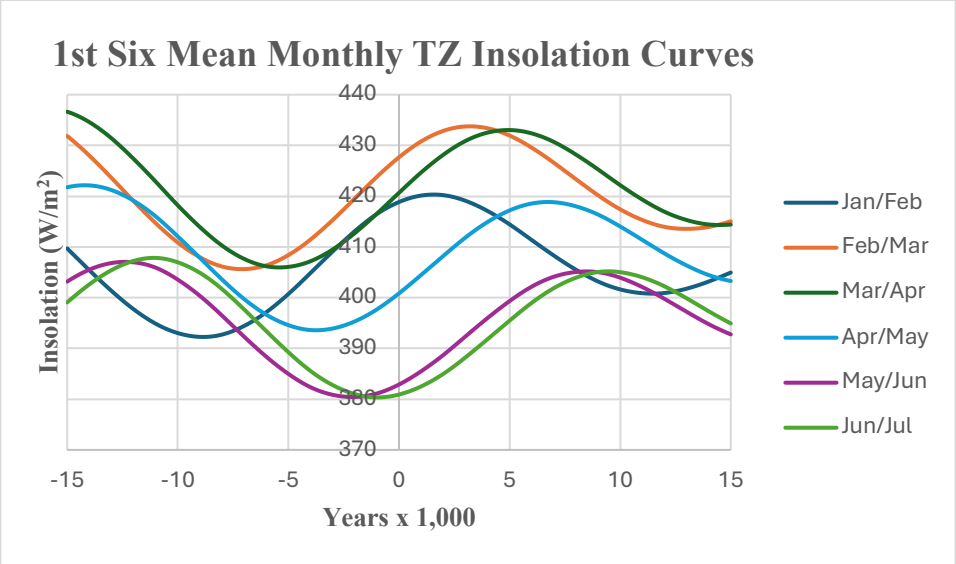

Figure 3. Six successive mean monthly insolation curves integrated over the TZ (-23.9343 to 23.9343 degrees latitude) using the computational method of Appendix A and variable days per monthly period described in Appendix B. There are six expected minima before t=0 due to the monthly periods 2-7 moving through aphelion. Note monthly periods 2-4 occur before -5 kyr, while 5-7 occur after. These two sets straddle aphelion along the orbital arc, with the Earth's axis tending to point perpendicular to the major axis of the elliptical orbit.

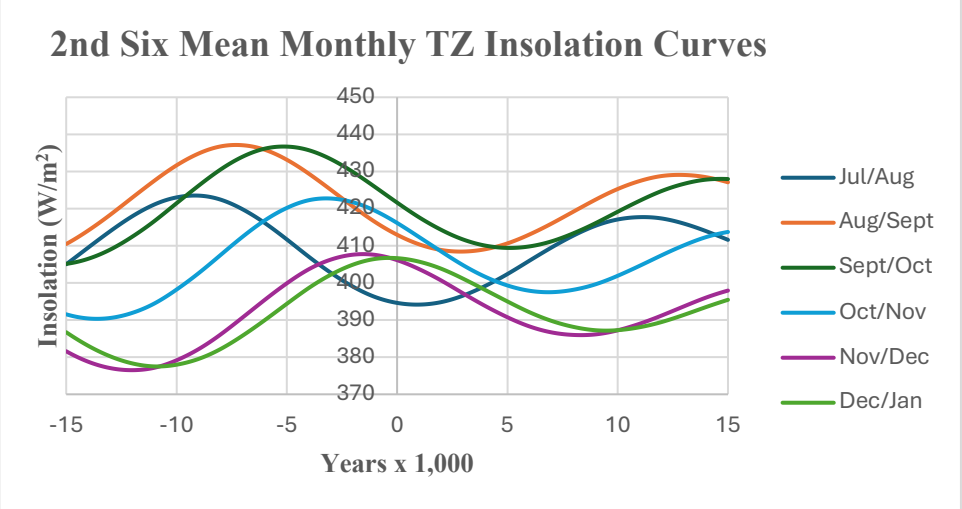

Figure 4. Six successive mean monthly insolation curves integrated over the TZ (-23.9343 to 23.9343 degrees latitude) using the computational method of Appendix A and variable days per monthly period described in Appendix B. There are six expected maxima before t=0 due to the monthly periods 8-12 +1 moving through perihelion. Note monthly periods 8-10 occur before -5 kyr, while 11,12+1 occur after. These two sets straddle perihelion along the orbital arc, with the Earth's axis tending to point perpendicular to the major axis of the elliptical orbit but opposite in direction to the aphelion set.

The two Figures have interesting features worth noting. In Figure 3, the six minima before t=0 cluster in two groups of three, with one group before -5 kyr and the other after. The same feature applies to Figure 4, but in this case to the maxima. What this indicates physically is that those six-monthly periods in the minima time window straddle aphelion, with the Earth's axis tending to point perpendicular to the major axis, and similarly those in the maxima window straddle perihelion with the axis pointing in the same direction.

To gain additional insight into these out-of-phase effects, we boxcar-average these insolation curves using equations (2.2) and (2.3), while taking account of the varying number of days per monthly period as described in Appendix B. Figure 5 presents the first and second six-monthly-period TZ insolation averages, H1 and H2, and the annual average.

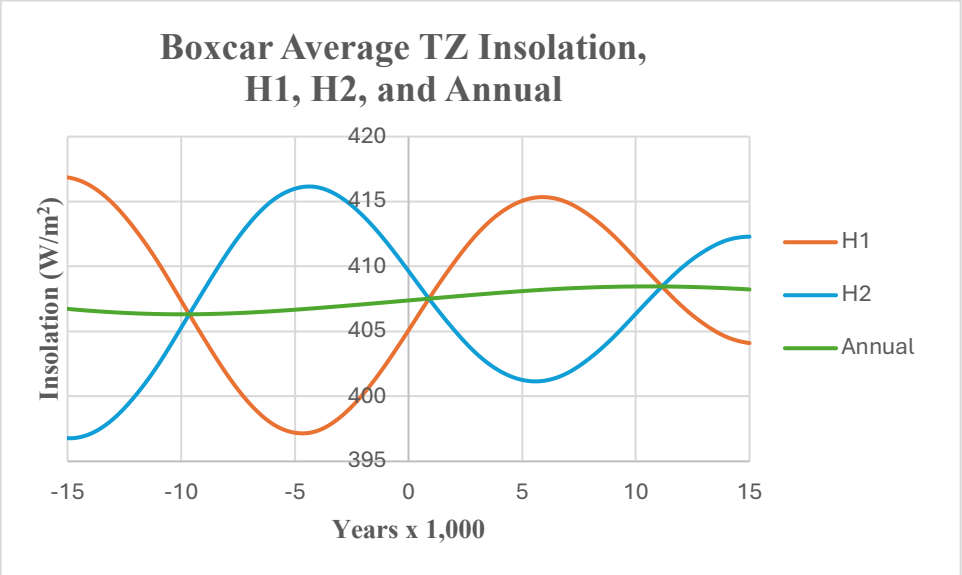

Figure 5. Applying equations (2.2) and (2.3) to the curves in Figures 3 and 4 generates the two channels, H1 and H2, that reveal an asymmetry, H2-H1, in the channels. The annual curve simply applies the boxcar averaging to the 12 monthly periods, resulting in a single, featureless channel that slowly increases over millennia.

As Figure 5 indicates, the out-of-phase asymmetry, H2-H1, is clearly muted by the annual average. H1 has a minimum value, 397.10 W/m^2, at -4.6 kyr and a subsequent maximum, 415.42 W/m^2, at +5.9 kyr, while H2 has a maximum value, 416.43 W/m^2, at -4.4 kyr and a minimum, 401.18 W/m^2, at +5.7 kyr. The H2-H1 asymmetry maximum is about 19 W/m^2 at -4.3 kyr. That magnitude is consistent with the percentage change in the Earth's insolation between aphelion and perihelion, 6.7 %, for the current orbit, having an average insolation of about 342 W/m^2. In the year 2000, this asymmetry was about 4.72 W/m^2, and in a later section, we will analyze how the Earth's climate system responds to this asymmetry using CERES data.

Both H1 and H2 are currently in linear regimes that will last about another 3,000 years. In Appendix C, we present a derivation of this linearity that is primarily due to the precession.

The minimum in H1 at -4.6 kyr provides a physically meaningful reference for determining changes in insolation and energy accumulation. The H1 and H2 insolation and energy-accumulation channels have contributed to the Earth's climate system prior to t=0. Because the Earth's climate system exhibits hysteresis effects through ocean heat content, the current climate is experiencing TZ energy-deposition effects that have accumulated over millennial timescales. However, our immediate interest is the behavior of these two separate channels for t≥0 to estimate the thermodynamically irreversible energy deposition from them. The insolation changes, ΔH1 and ΔH2, from the H1 minimum to its maximum are presented in Figure 6.

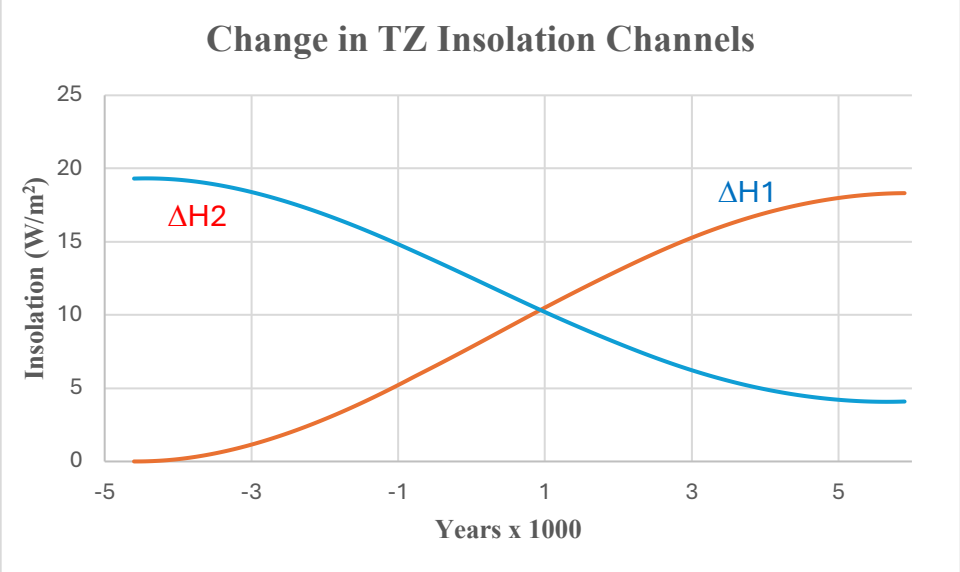

Figure 6. Here, the two channels, H1 and H2, are referenced with respect to the H1 minimum at -4.6 kyr resulting in ΔH1 and ΔH2, which when integrated using equations (2.4) and (2.5) results in the energy deposited into the TZ by the two channels.

The approximate linearity in ΔH1 will cause it to double from its value of 7.82 W/m^2 at t=0 in about 3,000 years, at a rate of about 2.3% per 100 years. In a similar manner, ΔH2 will be reduced from its t=0 value of 12.54 W/m^2 by 50% over approximately the same period, at a similar but negative rate. This behavior reverses in about 1,000 years, when the asymmetry H2-H1 is zero, meaning the radiation time windows become balanced with respect to the aphelion-perihelion orbital divide, and then H1 will dominate H2. Future changes in this asymmetry and the climate response to it can be monitored and measured through satellite observations, as discussed later.

The countervailing decline in AZ summer insolation is driven by the secular decline in obliquity and the movement of the summer solstice to aphelion, whereas AZ winter insolation remains relatively constant. This decline is also consistent with the Milankovitch Hypothesis, which posits a reduction in melt-season insolation suppression while maintaining cold winter temperatures for ice and snow accumulation. These insolation effects are depicted in Figures 7 and 8, where the AZ insolation is averaged over the summer monthly periods, 6-8. The decline in C1 from its maximum about 9,000 years ago to its minimum about 4,000 years from now is

quite substantial, exceeding 35 W/m^2. The C2 insolation, averaged over the winter monthly periods 12, 1, and 2, remains essentially constant over millennia and is a factor of 40 lower in magnitude than C1.

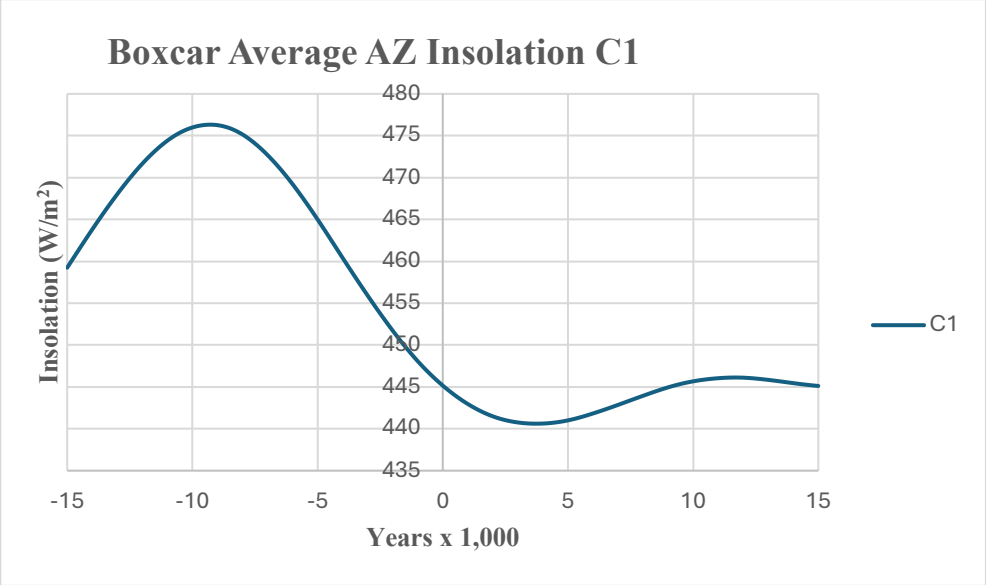

Figure 7. Three successive mean monthly period (6-8) insolation curves integrated using equation (2.1) over the AZ (60 to 90 degrees latitude) with the computational method of Appendix A and boxcar averaged using equations (2.2) and (2.3), including variable days per monthly period described in Appendix B. The decline from a maximum at about -9.3 kyr to the minimum at about +3.7 kyr is primarily due to the obliquity decline and, to a lesser extent, the movement of the summer solstice from perihelion to aphelion over a precession half-cycle.

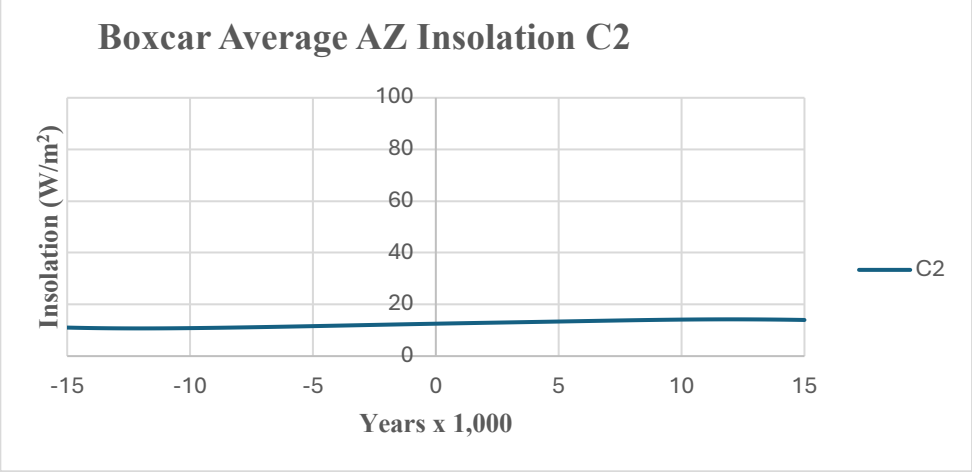

Figure 8. Three successive mean monthly (12,1, and 2) insolation curves integrated using equation (2.1) over the AZ (60 to 90 degrees latitude) with the computational method of Appendix A and boxcar averaged using equations (2.2) and (2.3), including variable days per monthly period described in Appendix B. The gradual increase is primarily due to the obliquity decline, and the movement of the winter solstice from aphelion to perihelion over about a precession half-cycle.

The C2-C1 AZ asymmetry has remained robustly negative for millennia, which supports the cryospheric nature of the AZ.

Together, Figures 9 and 10 below capture the countervailing aspect of COPE through the linear increase in the energy deposited in the TZ at the TOA, E_{H1}, obtained by integrating ΔH1 of Figure 6 over time, and the concurrent decline in C1 from the present represented by ΔC1, and the relative constancy of C2 represented by ΔC2, thereby reducing the AZ seasonal contrast between summer and winter. These physical attributes demonstrate that COPE accounts for the partitioning and distribution of isolation between the TZ and AZ on monthly-period and seasonal timescales in a countervailing manner.

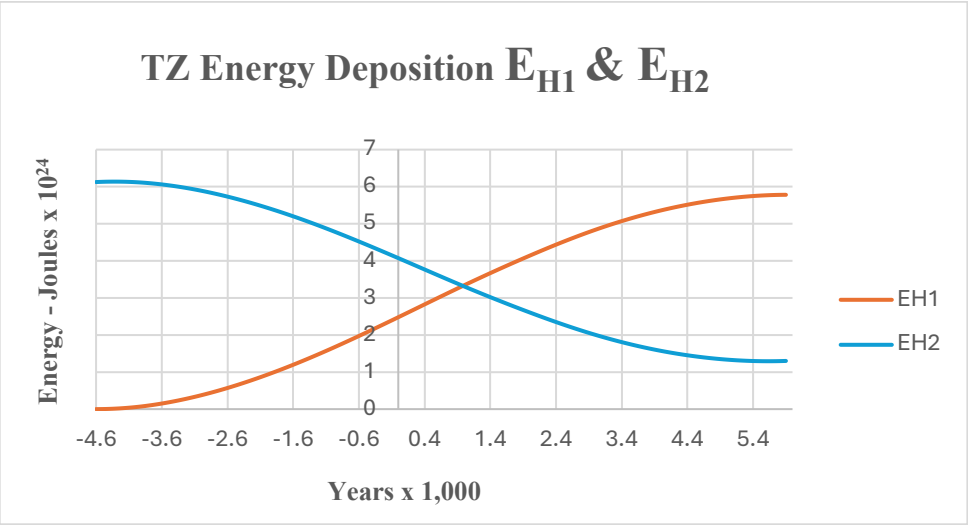

Figure 9. TZ Energy deposition channels E_{H1} and E_{H2} at the TOA from integrating the insolation channels, ΔH1 and ΔH2, in Figure 6.

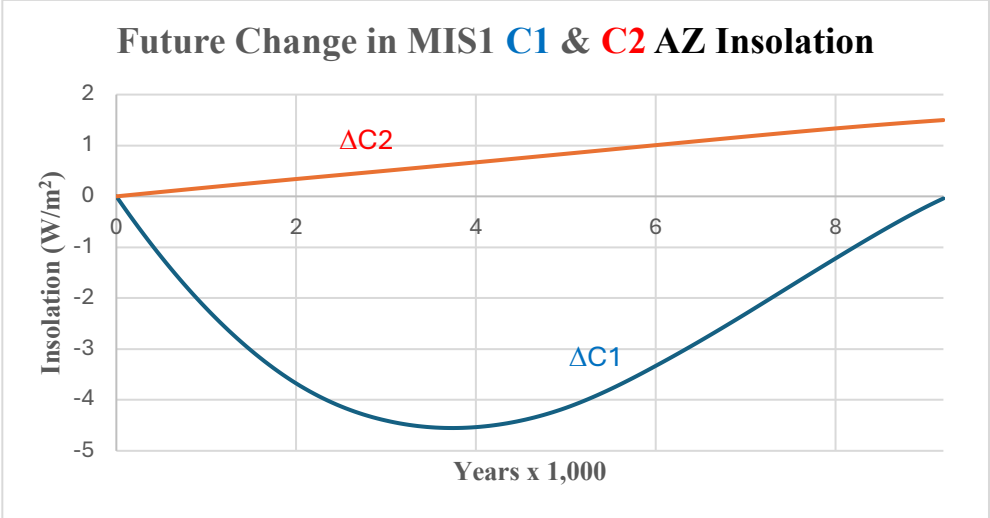

Figure 10. The future change in AZ boxcar-averaged insolation for channels C1 and C2 at the TOA, determined from Figure 7.

Traditional orbital theories emphasize reduced summer melt at high latitudes as the trigger of glaciation. However, sustained ice-sheet growth also requires a sufficient hydrological cycle to supply moisture to increase snowfall at high latitudes. COPE highlights how orbital geometry can simultaneously reduce Arctic melt potential while modulating tropical energy input, thereby influencing evaporation and poleward moisture transport.

---

5. Replication Across Interglacials: MIS1 vs MIS19

Several papers have indicated that the orbital solutions and insolation behaviors associated with MIS1and MIS19c are closely related. In this section, we expand that investigation by comparing the COPE behaviors of these interglacials. Figures 11 -13 demonstrate that, quantitatively, the COPE timing and amplitudes of seasonal and latitudinal insolation at the TOA for the TZ and AZ of MIS1 and MIS19c are very similar. This result deepens the connection and suggests that MIS1 could be a recurrence of MIS19c. Note that the insolation scale in Figure 13 is compressed by a factor of 40 compared to Figure 12, indicating that the C2 curves for MIS1 and MIS19c are essentially indistinguishable on the Figure 12 insolation scale.

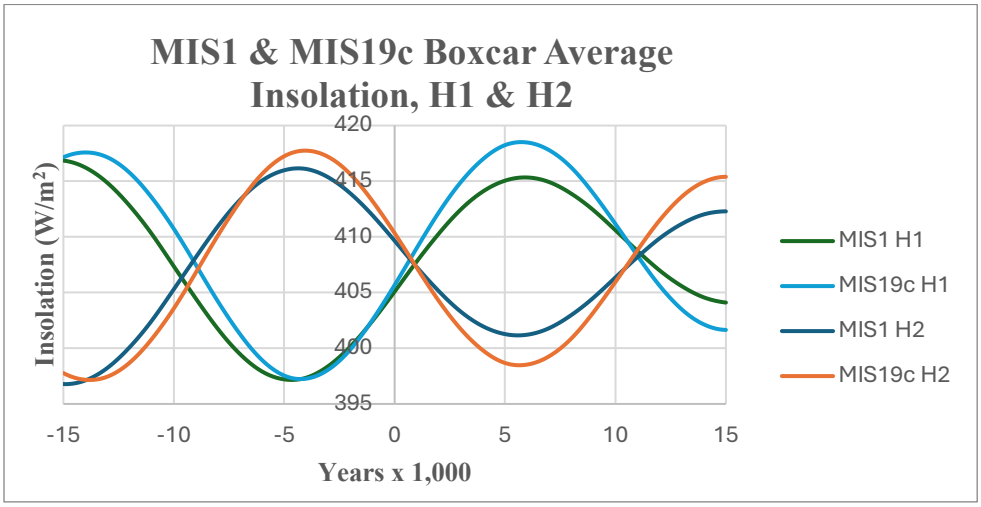

Figure 11. The comparison of the two insolation channels, H1 and H2, for MIS1 and MIS19c involving the monthly periods, 2-7 and 8-12 +1, and variable days as discussed in Appendix B.

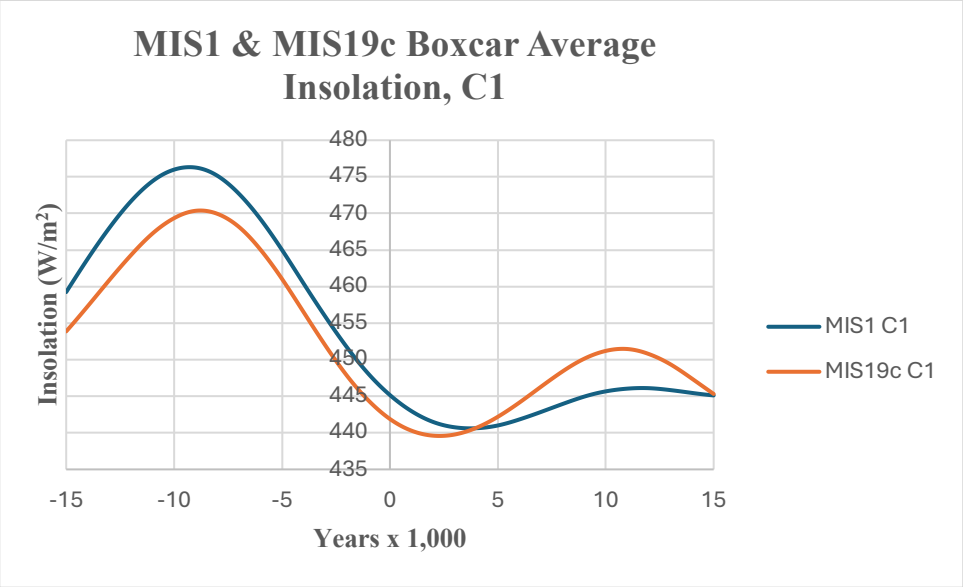

Figure 12. The comparison of the insolation channel, C1, for MIS1 and MIS19c involving the monthly periods, 6-8, and variable days as discussed in Appendix B.

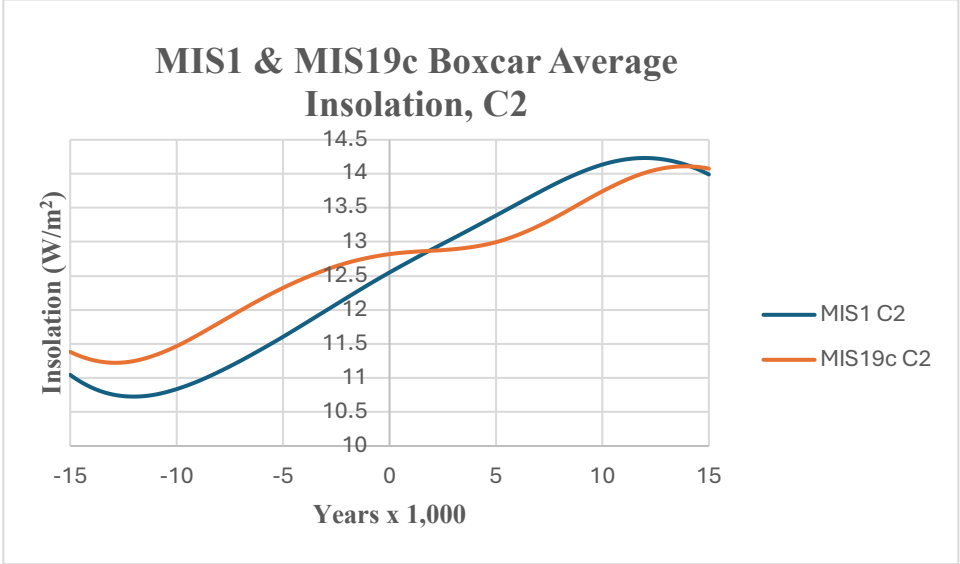

Figure 13. The comparison of the insolation channel, C2, for MIS1 and MIS19c involving the monthly periods, 12, 1, and 2, and variable days as discussed in Appendix B.

Furthermore, Figure 14 indicates that the heating from the H1 channel for MIS19c, E_{H1}, exhibits a steeper linear rise than that of MIS1; however, the MIS19c H2 channel shows a steeper linear descent. Meanwhile, Figure 15 addresses the AZ cooling comparison, in which the decline in MIS1 C1 is much deeper, nearly reaching -5 W/m^2, and lasts longer by about a factor of 2.

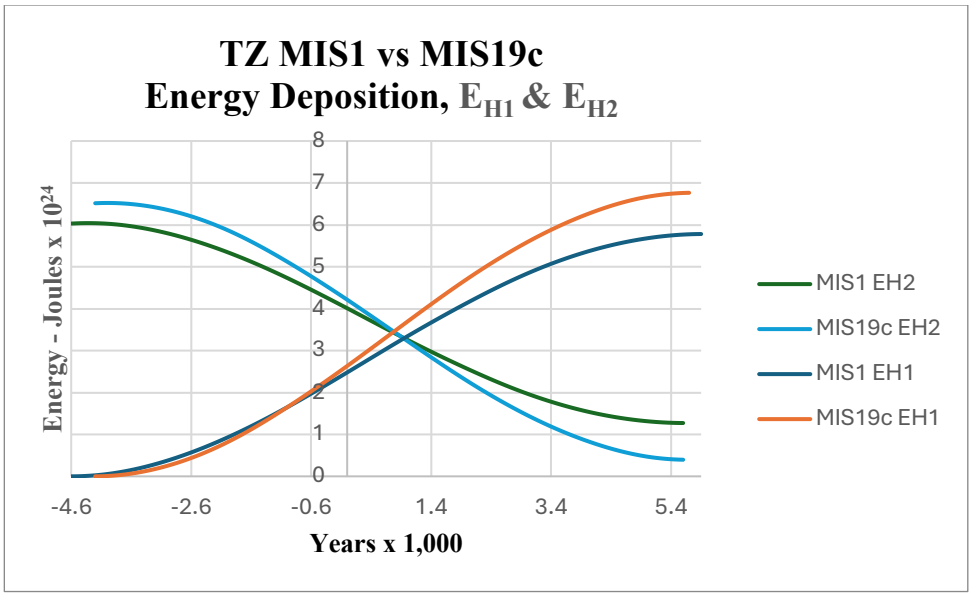

Figure 14. TZ MIS1 vs MIS19c Energy deposition channels E_{H1} and E_{H2} at the TOA from baselining each interglacial channel to its H1 minimum and integrating the insolation channels, ΔH1 and ΔH2 for each interglacial.

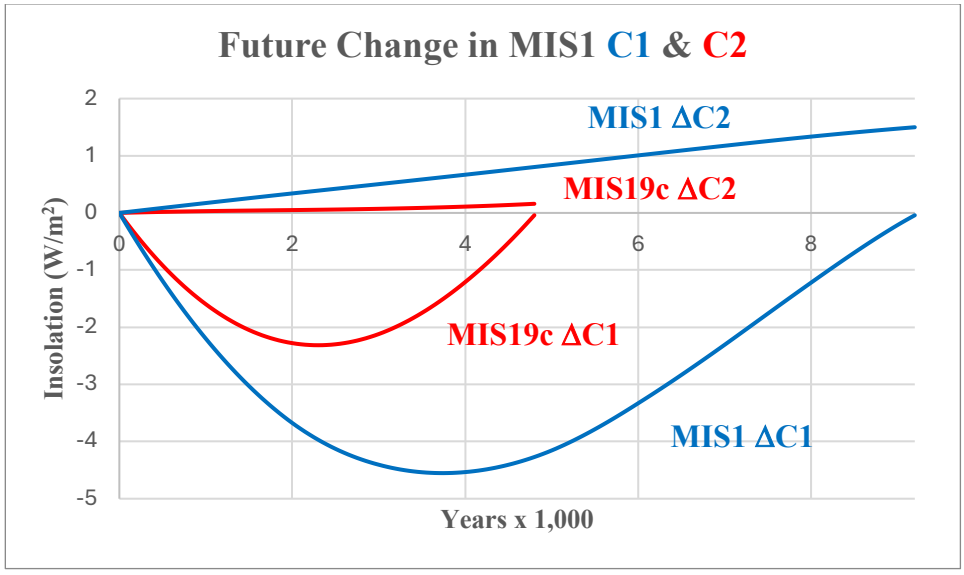

Figure 15. The comparison of the change in two insolation channels, ΔC1 and ΔC2, for MIS1 and MIS19c involving the monthly periods, 6-8 and 12,1 and 2, and variable days as discussed in Appendix B.

Figures 14 and 15 indicate that COPE is a common countervailing mechanism for these two interglacials.

Finally, we compare the energetic sufficiency for sea-level drawdown numbers associated with H1 and H2 for both MIS1 and MIS19c. We simply integrate under the curves in Figure 14. The energy deposited in the TZ area of 2.03 x 10^{14} m^2 at the TOA for the first channel, ΔE_{H1}, and the second channel, ΔE_{H2}, over the next 5,900 and 10,000 years for each interglacial is presented in

Table I below, where we use the TZ ocean area, which is about 0.7 of the total area. The total energy deposited at the TOA is about three times the energy required to lower the oceans by 400 ft in 5,900 years, and about five times that amount in 10,000 years. That is fairly robust in the absence of climate feedback mechanisms. Note that the numbers in red are to be multiplied by 10^{24} J. The MIS1 and MIS19c numbers are close, further emphasizing the similarity between the two interglacials, separated by about 800,000 years.

Table I: Energy Predictions for Sea Level Drawdown

MIS1 H1	MIS1 H2	TOTAL	Years
191	95	286	5,900
341	151	492	10,000
MIS19c H1	MIS19c H2		
210	75	285	5,700
389	114	503	10,000

MIS1 and MIS19c TZ energies at the TOA involving the channels H1and H2 and calculated from equations (2.4) and (2.5) while starting at t=0 to 5,900 years and 10,000 years, and including variable days per monthly period. The energy numbers are to be multiplied by 10^{24}J.

---

6. Does the COPE Asymmetry Survive Climate System Feedback Mechanisms?

The COPE framework predicts a distribution of solar energy between latitude zones and seasons while the global annual solar input remains nearly constant. A key question is whether the seasonal asymmetry predicted by COPE survives the radiative and dynamical adjustments of the Earth's climate system.

Incoming solar radiation was computed from orbital geometry using the solar constant (1,368 W/m^2) and the Sun–Earth distance derived from the Laskar orbital solutions (Laskar et al., 2004). Reflected shortwave radiation and outgoing longwave radiation were obtained from the CERES SYN1deg-Day Terra–Aqua–MODIS Edition 4B dataset (Loeb, N. et al., 2024), archived at the NASA Langley Atmospheric Science Data Center. This product provides daily global radiative fluxes on a 1°×1° grid, derived from CERES observations and MODIS cloud retrievals. Daily data were required because the analysis bins radiative fluxes into Laskar monthly periods defined by fixed 30° intervals of true solar longitude, rather than conventional calendar months. Because the duration of each solar-longitude interval varies slightly with orbital position through Kepler's Second Law, daily data allow the radiative fluxes to be weighted by the correct number of days within each Laskar monthly period. Radiative fluxes were spatially averaged over the TZ (23.4393°S–23.4393°N) and then aggregated into the seasonal channels: H1 (periods 2–7) and H2 (periods 8–12 + 1). Differences between these channels provide a direct observational test of the tropical seasonal asymmetry predicted by the COPE.

The CERES relevant metrics concerning the TZ asymmetry H2-H1 are presented in the following table:

Table II. Tropical Seasonal Channel Asymmetry (CERES)
H_1 = Laskar periods 2–7; H_2 = Laskar periods 8–12+1
Values represent $H_2 - H_1$ differences averaged over the Tropical Zone
Number of annual windows: 21 (2000 – 2021)

Metric	Physical Meaning	Mean (W/m^2)	Std Dev (W/m^2)	SEM (W/m^2)
ΔINSW	Difference in incoming solar radiation between seasonal channels	4.67	0.03	0.007
ΔRSW	Difference in reflected shortwave radiation	4.22	0.67	0.15
ΔASR	Difference in absorbed shortwave radiation	0.45	0.67	0.15
ΔOLR	Difference in outgoing longwave radiation	−0.54	0.58	0.13
ΔN	Net radiative imbalance retained by the climate system	0.99	0.70	0.15

Two sources of uncertainty must be considered in interpreting these results: measurement uncertainty in the CERES radiative fluxes and natural variability in the climate response.

Published assessments indicate that absolute uncertainties in CERES top-of-atmosphere radiative fluxes are on the order of 2–3 W m^{-2} for regional reflected shortwave and outgoing longwave fluxes, with smaller uncertainties in the global mean (Loeb et al., 2018). These uncertainties arise primarily from instrument calibration, radiance-to-flux conversion using angular distribution models (ADMs), and corrections for incomplete diurnal sampling inherent to polar-orbiting satellite observations (Loeb et al., 2003; Loeb et al., 2009; Loeb et al., 2018). Additional uncertainty arises from calibration stability and the use of imager-based cloud retrievals required for scene identification and diurnal cycle reconstruction (Su et al., 2020).

The present analysis focuses on differences between seasonal channels (H2 − H1) rather than absolute flux magnitudes. Because the dominant CERES uncertainties are largely systematic—principally calibration offsets, ADM assumptions, and diurnal sampling corrections—they act as common-mode biases that affect both seasonal intervals similarly. The differencing procedure, therefore, suppresses these systematic errors, rendering the resulting asymmetry primarily sensitive to relative seasonal variations rather than absolute radiative flux calibration.

Random errors and natural climate variability are further reduced through spatial averaging over the tropical zone and temporal averaging across the 21 annual windows examined. The interannual standard deviation of the net asymmetry is approximately 0.70 W m^{-2}. Averaging across the 21 windows reduces the random uncertainty in the mean by a factor of $1/N^{1/2}$, yielding a standard error of the mean of approximately 0.15 W m^{-2}. Thus, both random measurement noise and interannual variability are substantially reduced through multi-year averaging.

The CERES observations reveal a persistent seasonal asymmetry in tropical radiative fluxes consistent with the COPE framework. The incident orbital-seasonal forcing in the TZ at the TOA appears in the incoming shortwave term:

$$\Delta INSW \cong 4.7 - 4.6 \text{ W/m}^2$$

, with the range reflecting the predicted 0.1 W/m^2 decline from 2000 to 2021. The climate system responds to this forcing primarily through increased shortwave reflection by clouds and adjustments in longwave emission, represented by the ΔRSW and ΔOLR terms in Table II. These feedback mechanisms partially compensate for the imposed shortwave asymmetry.

Despite these adjustments, an average residual imbalance remains:

$$\langle \Delta N \rangle \cong 1 \text{ W/m}^2$$

indicating that a measurable fraction of the COPE asymmetry survives the radiative response of the climate system. Approximately four-fifths of the imposed shortwave asymmetry is offset by cloud reflection and longwave emission, while roughly one-fifth is retained within the tropical climate system.

Given the large ocean coverage of the tropical zone (~70%), this retained energy is most plausibly partitioned into ocean heat storage, evaporation, latent heat transport, and atmospheric circulation adjustments. These pathways provide a mechanism by which the orbital distribution of solar energy may influence the global hydrological cycle, the meridional temperature gradient, poleward moisture transport, and high latitude cryospheric evolution. It's important to note that COPE has been acting on the Earth's climate system for millennia.

The CERES observations, therefore, indicate that the seasonal asymmetry predicted by COPE is not fully eliminated by climate system feedback mechanisms; however, these feedback mechanisms arise from the incident H1 and H2 radiation fields. The average residual of 1 W/m^2 over the past two decades suggests that the zonal and seasonal distribution of solar energy produced by orbital geometry leaves a measurable signature in the modern climate system.

---

7. Summary and Discussion

This study identifies the Countervailing Obliquity–Precession Effect (COPE) as a mechanism that describes how orbital geometry distributes insolation and energy across latitude zones and seasons, while the global annual solar input remains nearly constant. The analysis shows that declining obliquity and the migration of the seasonal cycle relative to perihelion and aphelion jointly produce a countervailing distribution of insolation between the AZ and the TZ. As obliquity decreases and the summer monthly periods move through aphelion, summer monthly period insolation, C1, in the AZ declines, reducing the seasonal energy available for ice-sheet ablation, whereas AZ winter monthly-period insolation, C2, has remained relatively constant. This evolution is represented by a seasonal contrast, C2 – C1, that has been persistently negative and has decreased by more than 30 W/m^2 over the last 11, 000 years. At the same time, the

precessional migration of the seasonal cycle redistributes TZ insolation, manifesting as two seasonal channels, H1 and H2, whose relative magnitudes also evolve over time.

This orbitally driven distribution is muted in annual averages but becomes apparent when the tropical insolation field is analyzed according to monthly periods and grouped into biannual segments or channels. The resulting asymmetry metric, H2−H1, quantifies the difference in insolation between two tropical seasonal channels. Over the past several millennia, this asymmetry has evolved slowly as the seasonal windows have migrated along the orbit through precession. Since the Earth's climate system exhibits hysteresis, it is likely that past effects of COPE persist in the current climate system. Furthermore, the analysis shows that the tropical asymmetry reached a maximum of about 19 W/m^2 approximately 4.4 kyr before present and will gradually decline to zero over the next millennium as the H1 monthly periods approach perihelion; thereafter, the asymmetry will become negative, with H1 dominant rising linearly.

A comparison of the present interglacial, MIS1, with the orbital configuration of MIS19c, one of the closest orbital analogs in the late Pleistocene, shows that both interglacials exhibit similar COPE behavior. In each case, the tropical seasonal channel H1 experiences a minimum followed by a long-term increase as the seasonal cycle migrates toward perihelion. This similarity suggests that the zonal and seasonal distribution of energy associated with COPE may be a recurring feature of interglacial climates.

The observational analysis presented in Section 6 provides evidence that this distribution leaves a measurable signature in the modern radiation budget. Radiative fluxes from the CERES SYN1deg-Day Terra-Aqua-MODIS Edition 4B dataset were analyzed for the period 2000–2021 using Laskar monthly periods. The results show that the imposed tropical seasonal asymmetry in incoming shortwave radiation is partially offset by increased shortwave reflection and adjustments in longwave emission. Nevertheless, an average residual imbalance of

$$\langle \Delta N \rangle \cong 1 \text{ W/m}^2$$

remains in the tropical radiation budget. This residual indicates that a fraction of the COPE asymmetry survives the radiative and dynamical adjustments of the climate system. Given the large ocean coverage of the tropical zone, this retained energy is likely partitioned primarily into ocean heat storage, evaporation, and atmospheric transport processes that redistribute heat and moisture toward higher latitudes.

Over millennial timescales, the cumulative energy associated with the COPE distribution is substantial. Integrating the tropical energy surplus relative to $t \geq 0$ ($t=0$ corresponds to the year 2000) suggests that the total energy deposited in the tropical system since then is many times the energy required to lower global sea level by roughly 400 feet (~120 m). While the climate system responds to orbital forcing through complex feedback mechanisms among the atmosphere, ocean, and cryosphere, this energy accounting demonstrates that the distribution associated with COPE is sufficient to support the large-scale hydrological and cryospheric changes observed during glacial–interglacial cycles.

The results presented here, therefore, suggest that orbital forcing operates not only through high-latitude summer insolation but also through a broader distribution of solar energy across latitudes and seasons. The countervailing behavior of the AZ insolation and TZ energy budgets highlights the importance of considering the full spatial and seasonal structure of insolation when evaluating the climatic consequences of orbital variations.

Several avenues for future work follow naturally from this analysis. First, the analysis of the COPE mechanism could be extended to other interglacial intervals to determine whether similar zonal and seasonal energy distributions occur across the late Pleistocene record. In particular, analyzing other interglacials may help clarify the role of COPE in the timing of interglacial inceptions and terminations across the last 800,000 years, and help explain certain features in the ice-core and benthic time-series data.

Second, the interaction between the COPE and the climate system could be explored using numerical climate models. Because COPE constrains the spatial and seasonal distribution of solar energy, it provides input to how climate models redistribute radiative energy through clouds, atmospheric circulation, and ocean heat transport. Model experiments designed to track the fate of the COPE asymmetry could help determine how much of the redistributed energy is stored in the ocean, transported poleward, or returned to space through radiative feedback mechanisms.

Third, additional observational analyses may help clarify the climatic consequences of the COPE distribution. Satellite observations of radiation, cloud properties, atmospheric moisture, and ocean heat content could be examined to determine how the energy retained by the tropical asymmetry propagates through the climate system. Such studies may reveal whether the seasonal asymmetry influences large-scale circulation and precipitation patterns or the meridional transport of heat and moisture.

A potentially important observational test of the COPE framework is to determine whether poleward moisture transport into the Arctic exhibits a corresponding biannual asymmetry. Within the COPE framework, increased tropical-zone energy accumulation in the H1 seasonal channel enhances evaporation over tropical oceans, thereby strengthening the atmospheric branch of the hydrological cycle. Part of this additional moisture is transported poleward by large-scale atmospheric circulation and mid-latitude storm tracks, where it can contribute to snowfall and ice accumulation at high latitudes. Observational evidence already indicates an increase in cold-season snow and ice accumulation in parts of the Northern Hemisphere over recent decades. Satellite-based snow-cover observations compiled by the NOAA/Rutgers Global Snow Lab show increasing snow extent during autumn and winter months across Greenland and North America over approximately the past five decades (Robinson et al., 2012; Rutgers Global Snow Lab, 2024). A direct dynamical test would involve computing vertically integrated atmospheric moisture transport across high-latitude boundaries (e.g., 60° N) using modern atmospheric reanalysis datasets such as ERA5 (Hersbach et al., 2020) or MERRA-2 (Gelaro et al., 2017), which provide global fields of water vapor flux and vertically integrated moisture transport. The analysis could be performed over the modern satellite–reanalysis era beginning around 1979 and extending to the present. By binning the resulting moisture fluxes according to the H1 and H2 seasonal channels defined by the Laskar monthly periods, it would be possible to test whether

Arctic moisture import exhibits a systematic biannual asymmetry and whether this asymmetry evolves over time. Such an analysis would provide a direct empirical test of the proposed COPE linkage between tropical energy accumulation, enhanced evaporation, poleward moisture transport, and high-latitude snow and ice accumulation.

Taken together, the results presented here suggest that the countervailing distribution of insolation and solar energy associated with the COPE provides a useful framework for understanding how orbital variations influence the climate system. By linking orbital geometry, zonal insolation, and energy partitioning to modern satellite observations, the COPE framework offers a new perspective on the mechanisms by which orbital forcing may contribute to past glacial–interglacial climate transitions, as well as to the more recent aspects of the climate and its future evolution.

---

8. Acknowledgments

I have benefited on occasion from exchanges with ChatGPT and Gemini.

---

9. Appendices

Appendix A. Astronomical Framework and Insolation Calculations

The insolation calculations used in this study follow the astronomical framework developed by Laskar et al. (2004) together with the daily insolation formulation derived by Berger (1978). Orbital parameters (eccentricity, obliquity, and longitude of the perihelion) are taken from the astronomical solutions of Laskar et al., with time measured in 0.1 kiloyears relative to the epoch J2000 (t=0). The Laskar solution provides the time evolution of the orbital parameters governing Earth's insolation geometry, while the Berger formulation converts those orbital parameters into top-of-atmosphere solar radiation.

A.1 Orbital parameters

The orbital parameters required for the calculations are e(t), ε(t), and ϖ(t), where

e = orbital eccentricity
ε = obliquity of the ecliptic (axial tilt)
ϖ = longitude of perihelion measured from the vernal equinox

These parameters are obtained from the long-term astronomical solution of Laskar et al. (2004), commonly referred to as La2004. The solution provides tabulated values of the orbital elements as functions of time measured in kiloyears relative to the year 2000 CE.

The Laskar tables provide the quantities sin ϖ and cos ϖ from which the longitude of perihelion is determined using

$$\varpi = \operatorname{atan2}(\sin \varpi, \cos \varpi) \quad \text{(A.1.1)}$$

The two-argument arctangent ensures that the correct angular quadrant is selected.

A.2 Solar geometry

The seasonal position in Earth's orbit is described using true solar longitude, λ, measured from the vernal equinox. The solar declination δ is related to obliquity through

$$\sin \delta = \sin \varepsilon \cdot \sin \lambda \quad \text{(A.2.1)}$$

, where δ = solar declination.

The length of daylight at latitude φ is determined by the sunrise and sunset hour angles, $-H_0 \leq H \leq H_0$, where

$$H_0 = \arccos(-\tan \varphi \cdot \tan \delta) \quad \text{(A.2.2)}$$

, where φ = geographic latitude.

The total daylight duration is therefore proportional to $2H_0$, and the daily-mean insolation formulation integrates incoming radiation over this daylight interval.

A.3 Daily mean top-of-atmosphere insolation

Daily mean insolation is computed using the formulation derived by Berger (1978):

$$I(\varphi, \lambda, t)) = (S_0 / \pi)\,[(1 + e \cos(\lambda - \varpi))^2 / (1 - e^2)^2]\,[H_0 \sin \varphi \sin \delta + \cos \varphi \cos \delta \sin H_0] \quad \text{(A.3.1)}$$

, where

I = daily mean insolation
S_0 = solar constant = 1368 W/m^2
e = orbital eccentricity
ϖ= longitude of perihelion
λ = true solar longitude
δ = solar declination
H_0 = sunset hour angle
φ = latitude.

The factor, $(1 + e \cos(\lambda - \varpi))$, represents the variation of Earth–Sun distance produced by orbital eccentricity and precession.

A.4 Seasonal segmentation of the orbit

Following the convention used in Laskar et al. (2004), the annual cycle is partitioned into twelve intervals of true solar longitude, each spanning 30° with λ = 0 the vernal equinox (approximately March 21). These intervals are referenced in the Laskar tables using split calendar months. These split-calendar-month intervals are referred to as monthly periods throughout this paper to distinguish them from calendar months.

The twelve static approximations to the Laskar monthly periods are numbered thusly,

Monthly period approximate calendar intervals
1 Dec 21 – Jan 20
2 Jan 21 – Feb 20
3 Feb 21 – Mar 20
4 Mar 21 – Apr 20
5 Apr 21 – May 20
6 May 21 – Jun 20
7 Jun 21 – Jul 20
8 Jul 21 – Aug 20
9 Aug 21 – Sep 20
10 Sep 21 – Oct 20
11 Oct 21 – Nov 20
12 Nov 20 – Dec 21

The numbering begins with the Dec/Jan interval rather than the vernal equinox and ends with Nov/Dec. When seasonal averages span the end of the sequence, the numbering is treated cyclically, so that period 12 is followed by period 1.

The above monthly periods are approximate; however, because Earth's orbital velocity varies along its elliptical orbit, equal-longitude intervals correspond to unequal time intervals. Near perihelion, the Earth moves more rapidly, and the associated intervals contain fewer days; near aphelion, the intervals contain more days. Consequently, when multiple intervals are combined into seasonal averages, each interval is weighted by its duration. The computation of the interval durations is described in Appendix B.

The mean monthly period insolation in equation (2.1) is given by

$$Q_i(\emptyset, t) = \frac{1}{\Delta t_i} \int_{t_1}^{t_2} I(\emptyset, \lambda, t) \qquad \text{(A.4.1)}$$

, where the Δt_i are the interval durations associated with the variable monthly periods described in Appendix B.

Appendix B: Determination of Laskar monthly period durations

Monthly periods correspond to equal increments of true solar longitude

$$\Delta\lambda = 30^\circ \qquad \text{(B.1)}$$

, where $360^0 \geq \lambda \geq 0^0$ and the durations of these intervals depend on the orbital speed.

Let

$$\nu = \lambda - \varpi \tag{B.2}$$

where ϖ is the longitude of perihelion. The eccentric anomaly is the variable that connects the geometry of the ellipse to time through Kepler's equation

$$M = E - e \sin E \tag{B.3}$$

, where the eccentric anomaly, E, is given by

$$E = 2 \arctan \left(\sqrt{\frac{1-e}{1+e}} \tan \frac{\nu}{2}\right) \tag{B.4}$$

and time along the orbit is

$$t = \frac{M}{n} \tag{B.5}$$

, where $n = \frac{2\pi}{T}$ is the mean motion. Here, T is the orbital period of the Earth. For the purpose of converting the orbital intervals into civil time, T is taken to be the length of the tropical year,

$$T = 365.2422 \text{ days} \tag{B.6}$$

Thus, the elapsed time corresponding to a change in the mean anomaly is

$$t = \frac{T}{2\pi} M \tag{B.7}$$

For successive monthly-period boundaries i and i + 1, the duration of the monthly period, i, is therefore

$$\Delta t_i = T \frac{M_{i+1} - M_i}{2\pi} \tag{B.8}$$

which yields the variable number of days for each 30° orbital segment. By construction,

$$\sum_{i=1}^{12} \Delta t_i = T = 365.2422 \text{ days} \tag{B.9}$$

Appendix C: Origin of the linear time dependence of the insolation from the precession

The insolation may be written according to equation (A.3.1) is of the form

$$Q(\lambda, \emptyset) = \frac{S_0}{r^2} F(\emptyset, \lambda, \varepsilon) \tag{C.1}$$

where S_0 is the solar constant, r is the Sun–Earth distance in units of the semi-major axis, a, and F contains the projection and day-length factors depending on latitude ∅, true solar longitude λ, and obliquity ε.

For an elliptical orbit,

$$r = \frac{1-e^2}{1+e\cos(\lambda-\varpi)} \tag{C.2}$$

so that

$$\frac{1}{r^2} = \frac{(1+e\cos(\lambda-\varpi))^2}{(1-e^2)^2} \tag{C.3}$$

For small eccentricity, the leading precessional dependence is obtained by expanding to first order in e,

$$\frac{1}{r^2} \cong 1 + e\cos(\lambda-\varpi) \tag{C.4}$$

The eccentricity and the obliquity are very slow-changing functions over a precession half-cycle, so they are essentially constant, and the precession is also slowly varying, so it can be approximated by

$$\varpi \cong \varpi_0 + \dot{\varpi}\, t \tag{C.5}$$

, where $\dot{\varpi}$ is the precession rate. Expanding the cosine in equation (C.4) gives

$$\cos(\lambda - \varpi_0 - \dot{\varpi}\, t) = \cos(\lambda - \varpi_0)\cos(\dot{\varpi}\, t) + \sin(\lambda - \varpi_0)\sin(\dot{\varpi}\, t) \tag{C.6}$$

Since $\dot{\varpi}\, t \ll 1$ the last term provides the linear time dependence in equation (C.4), demonstrating that the precession drives the linear increase in H1 and the linear decrease in H2.

---

10. References

Berger, A. L. (1978), Long-term variations of daily insolation and Quaternary climatic changes, Journal of the Atmospheric Sciences, 35(12), pp. 2362–2367, https://doi.org/10.1175/1520-0469(1978)035.

Copernicus Climate Change Service (C3S) (2017 – present), ERA5: Fifth generation of ECMWF atmospheric reanalyses of the global climate, Copernicus Climate Change Service Climate Data Store (CDS), https://cds.climate.copernicus.eu.

Fairbanks, R. G. (1989), A 17,000-year glacio-eustatic sea level record: Influence of glacial melting rates on the Younger Dryas event and deep-ocean circulation, Nature, 342, pp. 637-642.

Gelaro, R., et al. (2017). *The Modern-Era Retrospective Analysis for Research and Applications, Version 2 (MERRA-2).*Journal of Climate, 30, pp. 5419–5454.

Hays, J.D., Imbrie, J., and Shackleton, N.J. (1976), Variations in the Earth's Orbit: Pacemaker of the Ice Ages, Science, Vol. 194, Issue 4270.
Hersbach, H., et al. (2020), The ERA5 global reanalysis, Quarterly Journal of the Royal Meteorological Society, 146, pp. 1999 – 2049.

Laskar, J., Robutel, P., Joutel, F., Gastineau, M., Correia, A. C. M., & Levrard, B. (2004), A long-term numerical solution for the insolation quantities of the Earth, Journal of Astronomy & Astrophysics, 428, pp. 261–285, https://doi.org/10.1051/0004-6361:20041335.

Loeb, N. G., et al. (2024), CERES SYN1deg-Day Terra-Aqua-MODIS Edition 4B data product, NASA Langley Atmospheric Science Data Center, DOI:10.5067/Terra+Aqua/CERES/SYN1deg-Day_L3.004B

Loeb, N. G., Kato, S., Loukachine, K., & Manalo-Smith, N. (2003), Angular distribution models for top-of-atmosphere radiative flux estimation from the Clouds and the Earth's Radiant Energy System instrument on the Terra satellite, Journal of Applied Meteorology, 42, pp. 240–265.

Loeb, N. G., Wielicki, B. A., Doelling, D. R., Smith, G. L., Keyes, D. F., Kato, S., Manalo-Smith, N., & Wong, T. (2009), Toward optimal closure of the Earth's top-of-atmosphere radiation budget, Journal of Climate, 22, pp. 748–766.

Loeb, N. G., Doelling, D. R., Wang, H., Su, W., Nguyen, C., Corbett, J. G., Liang, L., Mitrescu, C., Rose, F. G., & Kato, S. (2018), Clouds and the Earth's Radiant Energy System (CERES) Energy Balanced and Filled (EBAF) top-of-atmosphere (TOA) edition-4.0 data product. Journal of Climate, 31, pp. 895–918.

Milankovitch, M. (1941), Canon of insolation and the Ice-Ae Problem, Royal Serbian Academy Special Publication 132.

Parmentola, J.A. (2023), https://scienceofclimatechange.org/wp-content/uploads/Parmentola-2023-Celestial-Mechanics-Holocene-Termination.pdf

Robinson, D. A., Estilow, T., & NOAA Rutgers Global Snow Lab (2012). *Rutgers Global Snow Lab: Northern Hemisphere Snow Cover Extent Data.* Rutgers University Climate Lab. https://climate.rutgers.edu/snowcover

Rutgers Global Snow Lab (2024). *Northern Hemisphere Snow Cover Extent.* Rutgers University Global Snow Lab. https://climate.rutgers.edu/snowcover

Su, W., Corbett, J. G., Eitzen, Z. A., & Liang, L. (2020), Next-generation angular distribution models for top-of-atmosphere radiative flux estimation from CERES instruments: Methodology and evaluation, Atmospheric Measurement Techniques, 13, pp. 611–632.

11. Copyright and License

Parmentola, J. A. (2026). Countervailing Obliquity–Precession Effect: A Biannual Energy Asymmetry that Establishes Preconditions for the Climate System. Zenodo. https://doi.org/10.5281/zenodo.xxxxxxx